1 Title: Long-Term Inactivation of Sodium Channels as a Mechanism of Adaptation in CA1
2 Pyramidal Neurons

3 Abbreviated Title: Mechanisms of Adaptation in CA1 Pyramidal Cells

4 Author Names and Affiliations: Carol Upchurch[1]*, Crescent Combe[2]*, Christopher Knowlton[1],
5 Valery Rousseau[1], Sonia Gasparini[1,2]** and Carmen C. Canavier[1]**

6 [1]Department of Cell Biology and Anatomy, and [2]Neuroscience Center of Excellence, School of
7 Medicine, Louisiana State University Health Sciences Center, New Orleans, Louisiana, USA
8 70112

9 * co-first authors; ** co-last authors

10 Corresponding author: Sonia Gasparini, Neuroscience Center, Louisiana State University Health
11 Sciences Center, New Orleans, 2020 Gravier St., New Orleans, LA 70112, sgaspa1@lsuhsc.edu

12 Number of pages: 46 (including figures)

13 Number of figures: 8

14 Number of tables: 1

15 Number of words for Abstract: 250

16 Number of words for Introduction: 649

17 Number of words for Discussion: 1402

18 Conflict of interest statement: The authors declare no competing financial interests.

19 Acknowledgements: This work was funded by NIH R01 MH115832 under the CRCNS program
20 to CCC and SG.

Abstract

The hippocampus is involved in memory and spatial navigation. Many CA1 pyramidal cells function as place cells, increasing their firing rate when a specific place field is traversed. The dependence of CA1 place cell firing on position within the place field is asymmetric. We investigated the source of this asymmetry by injecting triangular depolarizing current ramps to approximate the spatially-tuned, temporally-diffuse depolarizing synaptic input received by these neurons while traversing a place field. Ramps were applied to rat CA1 pyramidal neurons *in vitro* (slice electrophysiology) and *in silico* (multi-compartmental NEURON model). Under control conditions, CA1 neurons fired more action potentials at higher frequencies on the up-ramp versus the down-ramp. This effect was more pronounced for dendritic compared to somatic ramps. We incorporated a five-state Markov scheme for $Na_V1.6$ channels into our model and calibrated the spatial dependence of long-term inactivation according to the literature; this spatial dependence was sufficient to explain the difference in dendritic versus somatic ramps. Long-term inactivation reduced the firing frequency by decreasing open-state occupancy, and reduced spike amplitude during trains by decreasing occupancy in closed states, which comprise the available pool. PKC activators like phorbol ester phorbol-dibutyrate (PDBu) are known to reduce Na_V long-term inactivation. PDBu application removed spike amplitude attenuation during spike trains *in vitro*, more visibly in dendrites, consistent with decreased Na_V long-term inactivation. Moreover, PDBu greatly reduced adaptation, consistent with our hypothesized mechanism. Our synergistic experimental/computational approach shows that long-term inactivation of $Na_V1.6$ is the primary mechanism of adaptation in CA1 pyramidal cells.

Significance statement (118 words)

The hippocampus plays an important role in certain types of memory, in part through context-specific firing of “place cells” that were first identified in rodents as cells that are particularly active when an animal is in a specific location in an environment, called the place field of that neuron. In this in vitro/in silico study, we found that long-term inactivation of sodium channels causes adaptation in the firing rate that could potentially skew the firing of CA1 hippocampal pyramidal neurons earlier within a place field. A computational model of the sodium channel revealed differential regulation of spike frequency and amplitude by long-term inactivation, which may be a general mechanism for spike frequency adaptation in the central nervous system.

Introduction

Area CA1 of the hippocampus is thought to play a key role in learning and memory, specifically episodic memories (Burgess et al., 2002), sequential order (Fortin et al., 2002; Hoang and Kesner, 2008) and trace conditioning (Shors, 2004; Hunsaker et al., 2006). A type of episodic memory involving the sequential order of places along a linear track has been well studied in rodents (O'Keefe and Nadel, 1978). Many CA1 pyramidal cells function as place cells (O'Keefe and Dostrovsky, 1971); they increase their firing rate as they traverse a place field. These fields are specific to a given environment (Colgin et al., 2008), and result from the activation of a particular subset of synaptic inputs by aspects of the place field in that environment. The firing rate of individual place cells is generally symmetric around a peak in the center of the place field, as recorded in head-restrained mice navigating a virtual spatial environment on a spherical treadmill (Harvey et al., 2009). However, intracellular recordings from the same mice revealed that traversing the place field evoked a depolarizing ramp of synaptic excitation that was not symmetric, but instead peaked after three quarters of the field had been traversed, such that the peaks of the firing rate and the underlying depolarization do not coincide. One explanation for this asymmetry is provided by the response of CA1 neurons to a temporally symmetric current ramp in anesthetized mice (Harris et al., 2002). The firing rate adapts such that the neuron fires substantially less on the down-ramp compared to the up-ramp. Such adaptation can explain how the firing rate peaks before the synaptic depolarizing ramp peaks. Although Harvey et al. (2009) observed a symmetric dependence of the firing rate on distance through the place field, this dependence becomes skewed in a predictive direction as the center of mass moves earlier in the place field as the environment becomes more familiar (Mehta et al., 2000), likely through synaptic plasticity mechanisms. Since adaptation is likely to contribute to the skew of the firing rate, here we investigate intrinsic mechanisms that determine firing rate adaptation in CA1 pyramidal cells.

Adaptation can result from accumulation of an outward current or a decrement in an inward current active in the inter-spike interval. The Ca^{2+}-activated small-conductance K^+ current (I_{SK})

79 (Stocker et al., 1999; Pedarzani et al., 2005) and the muscarinic M-type K^+ current (I_M) (Otto et
80 al., 2006; Gu et al., 2008) are often implicated in firing rate adaptation in CA1 pyramidal neurons.
81 Voltage-gated Na^+ channels in CA1 pyramidal neurons have previously been shown to exhibit
82 long-term inactivation that increases with distance from the soma along the apical dendrite
83 (Colbert et al., 1997; Jung et al., 1997), and the resulting decrease in the available pool of sodium
84 channels has been suggested as a mechanism for frequency adaptation in the same neurons
85 (Fernandez and White, 2010).

86 We systematically tested these possible mechanisms of adaptation using a combination
87 of *in vitro* slice electrophysiology and computational modeling. We applied symmetric current
88 ramps to the soma or apical dendrite of CA1 pyramidal cells to simulate the depolarizing synaptic
89 input these cells receive *in vivo* while crossing a place field. Selective blockers of I_{SK} and I_M did
90 not decrease adaptation. To investigate the putative contribution of long-term inactivation of Na^+
91 channels to adaptation in CA1 pyramidal neurons, we calibrated a Markov model of a Na^+ channel
92 with a second inactivated state that recovered more slowly than the first, according to the spatially-
93 dependent long-term inactivation shown in Mickus et al. (1999).

94 Experimentally, we observed that adaptation was more pronounced in the dendrites
95 compared to the soma. The model demonstrated that the increase in occupancy in the long-term
96 inactivated state of sodium channels along the apical dendrite was sufficient to account for this
97 difference. The application of a PKC activator, known to decrease occupancy in the long-term
98 inactivated state, significantly attenuated adaptation, as predicted by the model.

99

100 **Materials and Methods**

101 *Experimental methods*

102 *Slice preparation.* All the procedures described were conducted according to protocols
103 approved by the Louisiana State University Health Sciences Center-New Orleans Institutional

104 Animal Care and Use Committee, following guidelines on the responsible use of laboratory
105 animals in research from the National Institutes of Health. 7 to 11-week-old male Sprague Dawley
106 rats were deeply anesthetized via intraperitoneal injection of ketamine and xylazine (90 and 10
107 mg/kg, respectively). Once the toe-pinch and palpebral reflexes ceased, rats were transcardially
108 perfused with ice-cold oxygenated cutting solution containing, in mM: $NaHCO_3$ 28, KCl 2.5,
109 NaH_2PO_4 1.25, $MgCl_2$ 7, $CaCl_2$ 0.5, dextrose 7, sucrose 234, L-ascorbic acid 1, sodium pyruvate
110 3, and decapitated. The brains were rapidly removed and a vibratome used to cut 400 μm-thick
111 transverse hippocampal slices that were then transferred to a chamber filled with an oxygenated
112 artificial cerebro-spinal fluid (ACSF) containing, in mM: NaCl 125, $NaHCO_3$ 25, KCl 2.5, NaH_2PO_4
113 1.25, $MgCl_2$ 1, $CaCl_2$ 2, dextrose 25, ascorbate 1, sodium pyruvate 3. After the cutting procedure,
114 slices were allowed to recover for one hour at 36°C, with an additional recovery period of at least
115 one hour at room temperature.

116 *Patch clamp electrophysiology.* Individual slices were transferred to a submerged
117 recording chamber, and superfused with ACSF. All experiments were performed at 34-36°C. CA1
118 pyramidal cells were identified via differential interference contrast-infrared video microscopy.
119 Whole-cell current clamp recordings were made using Dagan BVC 700A amplifiers in the active
120 "bridge" mode. Recording pipettes had a resistance of 1-3 MΩ (for somatic recordings) and 3-5
121 MΩ (for dendritic recordings) when filled with an internal solution that contained, in mM: potassium
122 methanesulphonate 125, KCl 20, HEPES 10, EGTA 0.5, NaCl 4, Mg_2ATP 4, $Tris_2GTP$ 0.3,
123 phosphocreatine 14. Cells with resting membrane potentials depolarized beyond -60 mV at break-
124 in were discarded. Series resistance was monitored throughout the recordings and was usually
125 less than 20 MΩ; recordings were discarded when series resistance reached 25 MΩ or 30 MΩ,
126 for somatic and dendritic recordings, respectively.

127 NBQX (10 μM), DL-APV (50 μM), Gabazine (12.5 μM) and CGP55845 (1 μM) were applied
128 in the external solution in all experiments to block glutamatergic and GABAergic

129 neurotransmission, respectively, in order to isolate the contribution of the intrinsic ion channels to
130 the ramp responses. Apamin (100 nM), XE-991 (10 μM), phorbol-2,13-dibutyrate (PDBu, 5 μM),
131 and *Androctonus mauretanicus mauretanicus toxin 3 (*AmmTx3, 300 nM) were added to ACSF
132 as needed, from stock solutions made with water or DMSO; the concentration of DMSO in the
133 final solution was ≤ 0.1%. Gabazine and CGP55845 were purchased from Abcam (Cambridge,
134 MA), DL-APV and XE-991 were from HelloBio (Princeton, NJ), NBQX, apamin and AmmTx3 were
135 from Alomone Labs (Jerusalem, Israel), and PDBu was from Sigma (St. Louis, MO).

136 In order to approximate the depolarizing input that place cells receive as an animal
137 traverses the place field, symmetric ramp-shaped depolarizing current injections were applied via
138 the recording electrode to CA1 pyramidal neurons at either the soma or the apical dendrite (150-
139 250 μm from soma). Two second ramps (1 second up, 1 second down) and ten second ramps (5
140 seconds up, 5 seconds down) were delivered to simulate different running speeds. Current
141 amplitude was adjusted to evoke peak frequencies between 10 and 25 Hz that resemble place
142 cell firing as recorded *in vivo* (Hargreaves et al., 2007; Resnik et al., 2012; Bittner et al., 2015).

143 *Experimental design and statistical analyses*

144 Experimental data were recorded and analyzed with Igor Pro software (WaveMetrics).
145 Asymmetry of action potential firing with respect to the depolarizing ramp was quantified as a
146 spike ratio: the number of action potentials fired on the up-ramp divided by the number fired on
147 the down-ramp (Harris et al., 2002). Plots of instantaneous frequency versus current (f/I) use the
148 current value at the midpoint of the interspike interval (ISI). For experiments with PDBu, changes
149 in the rate of rise of the action potentials during a spike train were compared between conditions
150 by comparing the time derivative of the membrane potential dV/dt (Colbert et al., 1997), to
151 estimate the degree of attenuation of sodium conductance along the train. As most ramps evoked
152 at least 7 action potentials, a ratio was obtained of the maximum dV/dt for the 7th over the 1st
153 action potentials during the spike trains.

154 A typical patch clamp electrophysiology experiment with a difference in means of 1.3-2X
155 and a standard deviation of 0.2-0.3 requires n = 6-12 for p = 0.05 and a power of 0.9 (Cohen,
156 1977); each experimental group in this study is made up of n ≥ 9 recording sessions. The number
157 of cells recorded for each experiment is indicated in the Results section. Recordings were from
158 one cell per slice; in general, a maximum of three recordings were obtained for each animal.

159 Statistical analyses were performed in SPSS (IBM, RRID:SCR_002865), following the
160 tutorials and software guide from Laerd Statistics (2015, Statistical tutorials and software guides,
161 retrieved from https://statistics.laerd.com/). Where possible, comparisons were made in the same
162 cell before and after pharmacological treatment; the summary plots for these data include
163 individual points and means ± standard error of the mean. For these experiments, parametric
164 analyses (paired samples t-test and repeated-measures ANOVA) were used to compare
165 treatments in the same neurons, since data were normally distributed as determined by the
166 Shapiro-Wilk test for normality. Significant differences revealed by repeated measures ANOVA
167 were followed up by post-hoc analysis using Bonferroni-corrected pair-wise comparisons. In the
168 comparison between somatic and dendritic experiments, the Mann Whitney U test for unpaired
169 data was used, since the data were not normally distributed. In this case, the summary plot
170 consists of a box and whisker plot, including individual data. Differences were considered to be
171 statistically significant when $p < 0.05$.

172 *Computational modeling*

173 A multicompartmental CA1 pyramidal neuron model from our lab was used as a starting
174 point (Combe et al., 2018). This model was based on the (Poirazi et al., 2003a) model, with
175 subsequent changes made in Shah et al. (2008) and Bianchi et al. (2012). The
176 multicompartmental model from Combe et al. (2018) has 144 compartments in a reconstructed
177 morphology (Megías et al., 2001) (Figure 1A); each compartment can be represented with an
178 equivalent circuit (Figure 1B). Currents carried over from previous models include the leak

conductance, an A-type K^+ current (with different parameters for proximal and distal dendrites), a hyperpolarization-activated mixed cationic h-current, and T-type, R-type and L-type Ca^{2+} currents. Consistent with previous models, a 7-fold gradient in the h-conductance (Magee, 1998) and a 6-fold gradient in the A-type potassium conductance (Hoffman et al., 1997) were implemented along the apical trunk. In addition, in order to match the known lower amplitudes of back propagating spikes in the dendrites compared to the soma (Gasparini and Migliore, 2015), our model has a lower sodium conductance density in the dendrites compared to the soma (75% of the somatic value). The delayed rectifier in the previously cited models was replaced by separate models of K_v1 and K_v2 currents known to be present in CA1 pyramidal cells (Kirizs et al., 2014; Liu and Bean, 2014; Morgan et al., 2019). The K_v1 model was taken from Zbili and Debanne (2020) and the K_v2 model from https://senselab.med.yale.edu/ModelDB/showModel?model=184176. An inward rectifying potassium channel I_{KIR} was also added, consistent with the literature (Chen and Johnston, 2005): $I_{KIR} = \bar{g}_{KIR} \frac{(V-E_K)}{1+exp\left(\frac{V-E_K+8.2}{10}\right)}$. For the simulations in this work, I_M and I_{SK} were removed from the model for reasons explained in the text. In the previous model, intracellular calcium decayed with first order kinetics to baseline values. Calcium dynamics are not central to this study, but we incorporated the calcium balance module in Ashhad and Narayanan (2013) to make this model suitable for future extensions that will rely on calcium dynamics.

To better model long-term inactivation of $Na_V1.6$, the dominant somato-dendritic isoform in these cells (Lorincz and Nusser, 2010), the fast Hodgkin-Huxley-type Na^+ current was replaced in the apical dendrites and soma with a Markov model modified from Balbi et al. (2017). The original fast Hodgkin-Huxley-type Na^+ currents were retained in the axon and basal dendrites in the absence of any data regarding long-term inactivation in those regions. This Markov model has 5 states: 2 closed states (C1 and C2), an inactivated state (I1), a long-term inactivated state (I2) and an open state O (Figure 1D1). Current can only flow through the open state, and transitions between initial state *i* and final state *j* are governed by voltage-dependent equations in which a

Boltzman function is multiplied by a scale factor, R_{max}, specific to each transition rate, that gives the maximum transition rate. $R_{i\to j} = R_{\max} / (1+\exp(-(V-V_H)/V_S))$.

The O-I1 and I1-O transition rates are the sum of two scaled Boltzman functions; the parameters are reported in Table 1. To calibrate the Markov model, we simulated the experimental protocol described in Mickus et al. (1999). To replicate the cell-attached patch-clamp data therein, a simulated voltage-clamp was applied to a single-compartment iso-potential model containing only the Markov model of the Na^+ channel. The model was held at -65 mV, and a 20 Hz train of ten 2-ms square pulses depolarized to 50 mV from rest was applied. The percentage steady-state inactivation was calculated as the difference in current amplitude between the first pulse and the tenth pulse divided by the amplitude of the first pulse. The transition rate for entry from I1 to I2 was calibrated in different spatial compartments to reproduce the observed increase in percent steady state inactivation with distance from the soma along the apical dendritic trunk as shown in Mickus et al. (1999). The following monotonically increasing expression for the maximum rate for the I1 to I2 transition produced the steady-state inactivation shown in Figure 1D3, with x representing distance from the soma in μm: for x<49.4, $R_{\max} = 0.0299 + 0.0707(1-e^{-x/126})$, for 49.4<x≤124.1, $R_{\max} = 0.0091 + 0.1360(1-e^{-x/126})$, and for x> 124.1, $-0.0933 + 0.3(1-e^{-x/126})$. Compare Figure 1D2 containing the data (reproduced with permission from the original Elsevier source, Mickus et al. 1999) with simulations in Figure 1D3.

	C1-C2	C2-C1	C2-O	O-C2	O-I1	I1-O	C2-I1	I1-C1	C1-I1	I1-I2	I2-I1
R_{max}	12	0.5	14	4	0.5 , 2.5	5e-4 , 25e-5	0.06	0.2	0.2	*	36e-5
V_H	-8	-50	0	-48	-42 , 10	-42 , 10	-65	-65	-65	-25	-50
V_S	-10	9	-6	9	12 , -12	12 , -12	-11	10	-11	-5	12

Table 1: Parameters for transition rates between Markov states. The asterisk indicates a distance-dependent parameter as described in the text. R_{max} is in units of ms^{-1} and V_H and V_S are in mV.

The passive properties of the model were adjusted consistently with the literature. To account for the additional membrane area due to the higher density of dendritic spines at distal

227 dendritic sites (Megías et al., 2001), a spine factor was incorporated into the model that multiplied
228 the capacitance and divided the membrane resistance. This factor was 1.0 in the soma, the first
229 40 μm of the basal tree, and the first 100 μm of the apical trunk. In the apical tree, the factor
230 stepped to 2.0 at 100 μm, then increased with a linear dependence up to 3.5 at the point where
231 the apical dendrite branches into the tuft (394 μm in neuron pc2b). In the basal tree, the factor
232 stepped to 3.5 at 40 μm from the soma. These values were based on spine densities reported by
233 Megías et al. (2001). A sigmoidal decrease in membrane and axial resistance along the apical
234 dendrites was implemented to further account for the decrease in input resistance along the apical
235 dendrites (Magee et al., 1998; Poirazi et al., 2003b).

236 To replicate the experimental ramp protocol in the multicompartmental model, enough
237 current was injected in the model to hold the membrane potential at -60 mV, and all transients
238 were allowed to equilibrate before the application of the symmetric current ramp. These ramps,
239 of two and ten second durations, as described above, were applied in the soma, and at 219 μm
240 from the soma in the dendrites for the morphology in Figure 1A. The amplitude of the ramp was
241 adjusted to reach similar peak frequencies as in the experiments, 10 to 12 Hz in the long ramps
242 and 15 to 20 Hz in the short ramps. For the simulations, spike threshold was defined as the voltage
243 at which the second temporal derivative of the membrane potential exceeded 20 mV/ms^2.

244 *Software accessibility*

245 Model code is freely available and can be downloaded from ModelDB at:
246 http://modeldb.yale.edu/267140, access code: adaptationmodel.

247

248 **Results**

249 *In vivo* patch clamp recordings in rats on a linear track revealed that the synaptic input
250 received at the soma of CA1 pyramidal cells while traversing the neuron's place field resulted in

251 a hill-shaped depolarization above the baseline (Epsztein et al., 2011) that generally closely
252 followed the shape of the cell's firing rate. Since there were no defined, repeatable shapes of this
253 hill-shaped depolarization (Epsztein et al., 2011), in a first approximation to this spatially
254 modulated synaptic input, we injected symmetric triangular-shaped ramps, two or ten seconds in
255 total duration, either in the soma (Figure 2A), or in the apical trunk at ~200 μm from the soma
256 (between 140 and 240 μm, Figure 2B). The different durations could roughly correspond to
257 different running speeds. For the two second ramp in the soma (Figure 2A1), there are clearly
258 fewer spikes on the down-ramp compared to the up-ramp, which is quantified in the summary
259 data of the ratio of spikes on the up-ramp to spikes on the down-ramp in Figure 2C1. Moreover,
260 the inset that plots the instantaneous frequency versus the current (f/I) clearly shows hysteresis;
261 the frequency on the down-ramp is always slower than that on the up-ramp at the same average
262 level of depolarizing current. Concomitantly, firing initiates at a lower current amplitude than it
263 terminates. This type of f/I plot characterizes rate adaptation (Venugopal et al., 2015). The ten
264 second somatic ramps (Figure 2A2) show a similar pattern. The dendritic response to a two
265 second ramp (Figure 2B1) exhibits a much more pronounced decrease in spike height during the
266 train as well as more pronounced spike rate adaptation than the somatic ones. A Mann-Whitney
267 U test was run to compare the ratios of spikes on the up-ramp to spikes on the down-ramp
268 between somatic and dendritic injections, since the data were not normally distributed. For the
269 two second ramps, the distributions of the dendritic and somatic ratios were not similar, as
270 assessed by visual inspection. The ratio for dendritic ramps (mean rank 42.00) was significantly
271 higher than that for somatic ramps (mean rank 22.91), $U = 795$, $z = 4.129$, $p < 0.001$; Figure 2C1).
272 As with the shorter ramps, there is a much more pronounced decline in spike height in the
273 dendrites than in the soma during the ten second ramps; however, in this case a substantial
274 recovery of spike amplitude occurs on the down-ramp (Figure 2B2). The frequency, however,
275 does not recover on the down-ramp, indicating that these two aspects are regulated somewhat
276 independently, as we later demonstrate. A Mann-Whitney U test was run to compare the ratios of

spikes on the up-ramp to spikes on the down-ramp between somatic and dendritic injections for ten second durations, since the data were not normally distributed. In this case, the distributions of the dendritic and somatic ratios were similar, as assessed by visual inspection. Median ratio was significantly higher for dendritic than somatic ramps (2.12 vs. 1.66, U = 370, z = 3.019, p = 0.003; Figure 2C2).

Since the SK and M-type potassium currents are likely candidates to contribute to rate adaptation, we applied pharmacological blockers of each current separately and then together, and recorded responses in the apical dendrite where adaptation is most prominent (Figure 3). We have previously shown that the SK current prevents CA1 neurons from following fast (70-100 Hz) trains of Schaffer collateral stimulation but not 40 Hz stimulation (Combe et al., 2018). In this set of experiments with current ramp injections, the SK current blocker apamin (100 nM) did not occlude firing rate adaptation (Figure 3A) and the spike ratios were not significantly different (3.70 $\pm$ 0.67 under control conditions and 3.38 $\pm$ 0.62 in the presence of apamin, t(9) = -1.411; p = 0.192, n = 10, Figure 3D). The M-type K^+ channel blocker XE-991 (10 μM) caused the cells to fire faster at the onset of spiking (Figure 3B), but did not significantly affect the spike ratio (3.75 $\pm$ 0.74 under control conditions and 3.84 $\pm$ 0.72 in the presence of XE-991, t(8) = 0.434, p = 0.676, n = 9; Figure 3E). When both blockers were applied simultaneously, they still failed to occlude spike rate adaptation (Figure 3C); in fact, they appeared to enhance adaptation. Even with a lower amplitude current ramp, the firing frequency on the up-ramp was consistently high in the presence of apamin and XE-991, and cells tended to fire more action potentials on the up-ramp than they did in control. Thus, the spike ratio increased from 2.97 $\pm$ 0.28 in control conditions to 3.85 $\pm$ 0.47 in the presence of apamin and XE-991, t(10) = 2.349, p = 0.041, n = 11; Figure 3F). The voltage waveforms are different when both K^+ currents are blocked, in that the after-hyperpolarizations (AHPs) are shallower (see inset in Figure 3F). I_{SK} and I_M govern different parts of the AHP (Gu et al., 2005). When only one of them is blocked, the other appears to compensate to some degree.

302 When both are blocked, unconstrained spiking on the up-ramp significantly increases the spike
303 ratio.

304 The observations that adaptation is more pronounced in the dendritic than in the somatic
305 ramps, and that dendritic ramps show a prominent decrease in spike height along the train made
306 us hypothesize that the two features could be related. The decrease in spike height during the
307 train in the dendrites is known to be due to long-term inactivation of Na^+ channels (also called
308 slow, cumulative inactivation, see Colbert et al. (1997) and Jung et al. (1997); in order to add this
309 feature to our model, we replaced the fast Hodgkin-Huxley-type Na^+ current in the apical dendrites
310 and soma with a Markov model modified from Balbi et al. (2017, see Methods). The previous
311 studies in CA1 neurons often refer to slow, cumulative inactivation (Jung et al., 1997; Mickus et
312 al., 1999). We and others (Dover et al., 2010; Navarro et al., 2020) call this process long-term
313 inactivation instead, in order to differentiate it from a separate process called slow inactivation,
314 that requires seconds to develop (Fleidervish and Gutnick, 1996; Ulbricht, 2005). In contrast, the
315 long-term inactivated state is entered rapidly (within milliseconds) when fibroblast growth factor
316 homologous factors (FHFs) bind to cytoplasmic domains of voltage-gated sodium channels
317 (Goldfarb, 2012), but the recovery is slow, resulting in the longevity of the occupancy in the long-
318 term inactivated state. We therefore simulated the typical ramp responses recorded
319 experimentally under control conditions in this modified multicompartmental model containing the
320 Markov model for the Na^+ channel; we also omitted the M-type and SK currents, since the above
321 results indicated these currents did not substantially promote firing rate adaptation during the
322 triangular ramp protocol.

323 Figure 4A shows two and ten second simulated somatic ramps. The ratio of spikes on the
324 up-ramp to spikes on the down-ramp is ~2 for both ramps, and rate adapting f/I curves are also
325 observed (insets in Figures 4A1 and 4A2), making both the voltage traces and the f/I plots
326 qualitatively similar to those experimentally observed in Figure 2A. The state diagram plots

327 (Figures 4A3 and A4) show the fractional occupancy for each state of the Markov model for the
328 Na^+ channels, i.e. the fraction of channels that occupy a given state, as a function of time; a color
329 diagram of the transitions is shown as an inset at the right of Figure 4A4. By definition, the sum
330 of the fractional occupancy in all states is equal to 1. The color code at the right of Figure 4A3
331 orders the states in order of increasing availability to open. In general, channels must progress
332 from the fast-inactivated state (I1, orange) to the first closed state (C1, dark blue), then to the
333 second closed state (C2, cyan) before opening (O, green). The least available state is the long-
334 term inactivated (I2, magenta), since channels in this deeply inactivated state constitute a slow
335 pool that is not readily available. Transitions from I1 to the open state are allowed, but at an
336 extremely low rate (hence the red x indicating that this rate is very small in the inset in Figure
337 4A4), and transitions from C1 to the open state are not allowed (see Table 1). Therefore, in
338 general, channels must progress from I1 (orange) to C1 (dark blue) then to C2 (cyan) before
339 opening (O, green). The occupancy in the open state during the interspike interval (ISI) is too
340 small to be observed when plotted on the same scale as the other states. For the two second
341 ramp (Figure 4A3), occupancy in I2 accumulates during the spike train. Occupancy in I1 shows a
342 pronounced increase during each spike, but is diminished by the end of the spike train, because
343 a large fraction of channels become sequestered in I2.

344 Figure 4B shows two and ten second simulated dendritic ramps. The ratio of spikes on the
345 up-ramp to spikes on the down-ramp is ~3 for the short ramps and still ~2 for the longer ramp,
346 and rate adapting f/I curves were again observed (insets in Figures 4B1 and 4B2). The voltage
347 traces and f/I curves are qualitatively similar to the experimental observations in Figure 2B. For
348 short ramps, more adaptation is observed in the dendrites than in the soma. Notably, the
349 simulations also capture the substantially steeper decrease in spike amplitude in the dendrites
350 compared to the soma, consistent with the experimental observations in Figure 2. In addition, for
351 longer ramps, the simulations capture the partial recovery of spike height on the down-ramp, while

352 the frequency keeps decreasing (compare Figure 4B2 to Figure 2B). One important contrast
353 between the state diagram plots for somatic and dendritic current ramps is that for somatic ramps
354 occupancy in I1 is always higher than in I2, whereas during dendritic ramps the I2 occupancy
355 ends up exceeding that of I1. This is due to the spatial dependence of the parameter R_{max} that
356 determines the occupancy in the I2 state (see Methods and Figure 1D3), and largely accounts for
357 the differential effects of somatic versus dendritic current injection. Thus, the more prominent
358 effects on both spike frequency and amplitude reduction in the dendrites are due to the greater
359 build-up of occupancy in the I2 state in the dendrites as compared to the soma (compare magenta
360 traces in Figures 4A and B).

361 During the short ramps, occupancy in I2 accumulates until the end of the spike train; in
362 contrast, during the longer ramps, occupancy in I2 peaks and then declines before spiking ceases
363 (compare Figure 4B3 and 4B4). For these longer ramps, as the frequency slows on the down-
364 ramp, longer interspike intervals provide more time for long-term inactivation to be removed. For
365 sufficiently long intervals, more long-term inactivation is removed during the ISI than is added
366 during the preceding spike, allowing occupancy in I2 to decrease. As occupancy in I2 decreases,
367 occupancy in I1 increases, shifting a fraction of channels from the slow pool to the available pool.
368 The spike height, which decreases during the up-ramp because long-term inactivation is
369 accumulating, recovers to some degree on the down-ramp, as occupancy in the I2 state starts to
370 decrease. However, the frequency does not recover; in fact, it slows down even more as the spike
371 height recovers. Our working hypothesis was that occupancy in the I2 state is responsible for both
372 the decrease in spike height and the decrease in frequency; therefore, it was not immediately
373 evident how these two quantities could be differentially regulated by occupancy in the I2 state.

374 An explanation for these counterintuitive findings comes from the observation that, as I2
375 occupancy decreases and I1 occupancy increases during the long ramps, occupancy in C1
376 increases as well (see dark blue trace in Figure 4B4). This suggests that the closed states, as

377 part of the readily-available pool, may play a role in the differential recovery of spike height and
378 frequency. We looked more closely at the occupancy in various states during the longer ramps,
379 using spike height as an additional measurement, and compared the differences between somatic
380 and dendritic ramps by superimposing occupancy in the various states for the same levels of
381 injected currents in the up- and down-ramps (Figure 5). These plots show that occupancy in each
382 of the states follows a history-dependent (hysteretic) trajectory. If there were no hysteresis,
383 occupancy on the up- and down-ramps at the same level of applied current would be identical.
384 Figure 5A shows that the occupancy in the immediately available pool, consisting of channels in
385 the C1 and C2 closed states (Baranauskas and Martina, 2006), is generally lower during the
386 down-ramp than the up-ramp at comparable values of injected current. The hysteresis is more
387 pronounced for the dendritic injections (Figure 5A2); moreover, the occupancy in the readily
388 available states is, in general, lower in the dendrite than at the soma. At spike threshold, only the
389 channels in the available pool (C1+C2 states) can be regeneratively recruited for the action
390 potential upstroke. Therefore, in Figure 5B we plotted the spike height versus occupancy in the
391 C1+C2 pool at spike threshold. The height was measured from threshold to peak in order to
392 exclude contributions of the AHP to spike amplitude. Occupancy in the C1+C2 pool accurately
393 predicted spike height, independent of whether injected current was increasing (up-ramp, filled
394 circles) or decreasing (down-ramp, open circles), both for the soma (Figure 5B1) and for the
395 dendrites (Figure 5B2). However, the dependence of the spike height on C1+C2 occupancy was
396 much steeper in the dendrites than in the soma suggesting that a smaller change in C1+C2
397 occupancy can yield a larger difference in spike height during the spike train. Together with the
398 larger hysteresis in occupancy states in the dendrites, this largely explains the greater decrement
399 in spike height in the dendrites.

400 Given the dependence of dendritic spike height on the available pool in C1+C2, it is clear
401 that the spike height in Figure 4B2 recovers during the down-ramp because C1+C2 is increasing

on the down-ramp (Figure 5A2), largely due to increases in C1 (dark blue trace in Figure 4B2), which is generally in equilibrium with I1. Recall that the decrease in I1 (and consequently C1+C2) is driven by the cumulative increase of occupancy in the slow pool (I2), as shown in Figure 4. We therefore looked at the occupancy in I2 for the superimposed up- and down-ramps. Again, the hysteresis is more prominent in the dendrites (Figure 5C2) than the soma (Figure 5C1). The differential regulation of the spike height and frequency by occupancy in the I2 state occurs in part because the frequency does not depend directly upon occupancy in C1+C2, which increases even as the frequency has yet to recover. Instead, the frequency depends on the very small fractional occupancy in the open state during the interspike interval (Figure 5D, with values during spikes removed). Occupancy in the open state during the interspike interval is generally lower for both soma (Figure 5D1) and dendrite (Figure 5D2) on the down-ramp compared to the up-ramp at comparable values of injected current, but again the effect is more prominent in the dendrite. Occupancy in the open state during successive interspike intervals also increases (but only slightly) on the down-ramp for the same reason the available pool increases, namely the decrease in occupancy in I2. However, the frequency, unlike the spike amplitude, does not depend solely on the occupancy in the states of the Markov model, but also on the injected current. Therefore the frequency does not recover because occupancy in the open state, although it increases during the down-ramp, is still below the values on the up-ramp, so the small increase is not sufficient to compensate for the constantly decreasing level of injected current on the down-ramp. Moreover, spiking ceases at higher values of injected current on the down-ramp than those that were required to initiate spiking on the up-ramp. A Markov model that differentiates between a fast and a slow pool as well as differentiating between a readily-available pool and the fast-inactivated pool easily accounts for this differential regulation of spike frequency and spike height, whereas we were never able to obtain these results with Hodgkin-Huxley type models. Our model describes well both frequency and height changes; the differential regulation of these two quantities initially appears counterintuitive and would be difficult to tease out experimentally.

428 In order to show that asymmetry and spike rate adaptation in the f/I plots in the model are
429 unequivocally due to occupancy in the long-term inactivated state (I2), we ran simulations with
430 entry into that state blocked (Figure 6A and B). These simulations confirm that firing rate
431 adaptation in the model is indeed due to this mechanism; the f/I plots cease to show any
432 hysteresis and become linear instead, both for somatic (Figure 6A) and dendritic current injections
433 (Figure 6B). Similar results were obtained with two additional morphologies (c80761 from Ishizuka
434 et al. (1995) and pc1a from Megías et al. (2001); see extended data in Figures 6-1 and 6-2,
435 respectively), to verify that this mechanism could be generalized. Since the model strongly
436 suggests that spike rate adaptation is due to long-term inactivation of the sodium channels, and
437 since phosphorylation by protein kinase C (PKC) has been shown to reduce long-term inactivation
438 of dendritic Na^+ channels (Colbert and Johnston, 1998), we attempted to reduce occupancy in the
439 long-term inactivated state in CA1 neurons *in vitro* by applying a PKC activator, the phorbol ester
440 phorbol-di-butyrate (PDBu, Figure 6C and D). As predicted, both somatic and dendritic ramps
441 exhibit far less rate adaptation in the presence of PDBu compared to control. PDBu (5 μM)
442 decreased the spike ratio in the soma (Figure 6C and E) from 2.31 ± 0.22 in control conditions to
443 1.37 ± 0.09, $t(10) = -5.071$, $p < 0.001$, $n = 11$). PDBu also prevented the reduction in spike
444 amplitude during dendritic ramps, consistent with an effect exerted via reducing long-term
445 inactivation of sodium channels (Colbert and Johnston, 1998). In addition, the spike ratio for the
446 dendritic recordings decreased from 3.48 ± 0.46 to 1.64 ± 0.16, $t(9) = -4.278$, $p = 0.002$, $n = 10$,
447 Figure 6D and F).

448 Since there are other targets of phosphorylation by PKC, most notably the A-type
449 potassium current carried by Kv4.2 channels, which is expressed at higher densities in the
450 dendrites of CA1 neurons (Hoffman et al., 1997; Hoffman and Johnston, 1998), we performed an
451 additional set of experiments to rule out a contribution of the A-type current to the occlusion of
452 firing rate adaptation and asymmetry. Figure 7 shows that the specific Kv4 blocker *Androctonus*

453 *mauretanicus mauretanicus toxin 3* (AmmTx3, 300 nM) by itself has little effect on spike frequency
454 adaptation or spike height (compare Figure 7B to 7A). When added in the presence of AmmTx3,
455 PDBu 5 μM still substantially reduced spike rate adaptation (Figure 7C) as quantified by the spike
456 ratio (Figure 7E) and prevented the decrease in spike amplitude during a train. The spike ratio
457 was significantly different across the three conditions according to a one-way repeated measures
458 ANOVA ($F(2,16) = 9.231$, $p = 0.002$). Bonferroni-corrected post-hoc pairwise comparisons found
459 no significant changes between the spike ratios under control conditions (3.46 ± 0.57) and in the
460 presence of AmmTx3 (3.79 ± 0.68, $p = 0.877$), but a significant decrease in the presence of PDBu
461 (1.86 ± 0.16), with $p = 0.039$ and 0.034, respectively, for $n = 9$. Figure 7D shows the profile of the
462 rate of rise (dV/dt) of the dendritic voltage traces. The maximum rate of rise corresponds to the
463 early part of the action potential and is dependent on the available Na^+ conductance (Fleidervish
464 et al., 1996; Colbert and Johnston, 1998); the decrease in these peaks mirrors the decrease in
465 spike amplitude along the action potential train evoked by the ramp. The maximum rate of rise
466 decreased significantly along the train due to the progressively decreased availability of Na^+
467 channels during the train under control conditions and in the presence of AmmTx3, but far less in
468 the presence of PDBu (Figure 7F). A one-way repeated-measures ANOVA found that the ratio
469 between the 7th and the 1st dV/dt was significantly different between the three conditions
470 ($F(1.102,8.819) = 134.262$, $p < 0.001$, $n = 9$). Bonferroni-corrected pairwise comparisons found
471 no differences between control conditions (0.49 ± 0.04) and in the presence of AmmTx3 ($0.49 \pm$
472 0.04, $p = 1.00$), but a significant increase in the presence of PDBu (0.83 ± 0.02, $p < 0.001$),
473 suggesting a significant activity-dependent decrease in the fast sodium current in control and
474 AmmTx3, that is prevented by PKC activation with PDBu. On the other hand, AmmTx3 clearly
475 exerted an effect by broadening the AP (Figure 7G) as expected, given the important contribution
476 of I_A via Kv4.2 channels to spike width in these neurons (Kim et al., 2005). These results support

477 our model prediction that entry of Na_V channels into the long-term inactivated state promotes firing
478 rate adaptation in response to symmetric depolarizing input.

479

480 **Discussion**

481 *Summary*

482 In this study, we have shown that 1) experimentally observed adaptation in response to
483 depolarizing ramps is more prominent in the dendrites than the soma, 2) adaptation is not
484 mediated by the M-type and SK K^+ currents that mediate adaptation in other conditions, 3)
485 adaptation is likely mediated by long-term inactivation of sodium channels, and 4) a
486 phenomenological five-state Markov model calibrated with a distance-dependent long-term
487 inactivation can account for the differences in adaptation between soma and dendrite, as well as
488 for the differential regulation of spike height and frequency by long-term inactivation.

489 *Significance*

490 Since the excitatory inputs that mediate spatially-tuned firing of place cells are likely
491 received in the dendrites, the adaptation mediated by long-term inactivation of Na^+ channels that
492 we observe in the dendritic ramps likely affects the position of the center of mass of place fields,
493 with implications for spatial coding. This study was performed in the context of a sustained
494 depolarization that is thought to underlie activation of ensembles of CA1 place cells. However,
495 the sequential activation of place cells along a linear track likely generalizes to sequential
496 activation encoding other types of episodic memory (Wood et al., 1999), meaning that these
497 findings may be important for understanding episodic memory in general. Also, gain control
498 (Chance et al., 2002), or modulation of the slope of the frequency-current input-output relationship
499 of a neuron, is a general feature of neural processing (Salinas and Thier, 2000); the spike
500 frequency adaptation modulated by Na_V long-term inactivation is a form of divisive gain control as

501 sustained depolarization, and the consequent adaptation, can decrease the slope of the steady-
502 state frequency-current relationship (Fernandez and White, 2010).

503 *Previous work on long-term inactivation of Na_V channels in CA1 pyramidal cells*

504 This work bridges the work by Fernandez and White (2010) using somatic recordings to
505 suggest that long-term inactivation of sodium channels is responsible for frequency adaptation
506 and the work by Colbert et al. (1997, 1998) showing that slow sodium channel recovery from
507 inactivation is responsible for a decrease in amplitude during a train of dendritic back-propagating
508 action potentials. Our modeling work unifies these phenomena with a common mechanistic
509 explanation of how these two processes are differentially regulated.

510 *Essential aspects of the phenomenological Markov model*

511 Much more complicated Markov models of NaV gating exist (Goldfarb, 2012; Navarro et
512 al., 2020), but we attempted to use the simplest model possible to gain insight into long-term
513 inactivation. We started with a published six-state model (Balbi et al., 2017) and removed one
514 open state (Knowlton et al., 2021) leaving the five-state model as in Figure 1D1. Figure 8
515 recapitulates the main features of the model and how the various states/pools differentially
516 regulate adaptation and spike height during the train. The first essential aspect of the model is
517 that the slow pool (represented by a single state, I2, indicated in magenta in Figure 8) sequesters
518 a fraction of the Na_V channels and renders them completely unavailable for hundreds of
519 milliseconds. Channels are recruited into this state during a spike and recover slowly during the
520 interspike interval (see Figure 4), allowing accumulation across multiple spikes. The choice to
521 connect I2 to the fast pool via I1 rather than O, as some models do (Goldfarb, 2012; Navarro et
522 al., 2020), is not fundamental but phenomenological and inherited from Balbi et al. (2017). The
523 second essential aspect of the model is that the fast pool is not monolithic but separated into three
524 conceptual pools: the fast-inactivated (I1) pool, the readily available (C1+C2) pool and the open
525 pool. Therefore, including I2, a minimum of four pools of NaV channels is required to explain our

526 results. Since the transition from C1 to C2 is fast, these closed states (indicated in shades of blue
527 in Figure 8) are immediately available to be recruited into a regenerative, positive feedback loop
528 that drives the spike upstroke, and as shown in Figure 5B, the occupancy in this pool uniquely
529 determines spike height. The I1 fast-inactivated state constitutes its own pool (orange in Figure
530 8); it is not available immediately prior to a spike but can be quickly recruited into the available
531 pool during the after-hyperpolarization and contribute to the following spike. Finally, the open pool
532 (indicated in green in Figure 8) has up to 20% occupancy during spiking, but in the order of 0.01%
533 during the interspike intervals, as shown in Figure 5D. The slow pool has more occupancy on the
534 down-ramp than on the up-ramp at comparable values of injected current, due to the history of
535 depolarization, therefore by a material balance the fast pool must have less occupancy on the
536 down-ramp. We have shown that although hysteresis in I2 drives both decreases in spike height
537 and in frequency, these aspects are differentially regulated by the available and open pools,
538 respectively. As shown in Figure 4, the long-term inactivated state is entered quickly during a
539 spike, and, if the subsequent interspike interval is too short to remove the amount of long-term
540 inactivation induced by the spike, inactivation accumulates. However, for sufficiently long
541 intervals, more long-term inactivation is removed during the ISI than is added during the preceding
542 spike, allowing occupancy in the long-term inactivated state to decrease. As a consequence,
543 occupancy in the readily available (C1+C2) pool increases, allowing spike height to recover
544 somewhat on the down-ramp. In contrast to the complete dependence of spike height on the
545 available pool, frequency depends not only upon the hysteresis in the open pool, but also on the
546 injected current. Therefore, spike height can recover to some degree on the down-ramp while the
547 frequency is still decreasing.

548 *Contributions of SK and M-type potassium currents*

549 Previous work has implicated the SK and M-type K^+ currents in spike frequency adaptation
550 in CA1 pyramidal cells (Madison and Nicoll, 1984; Aiken et al., 1995; Peters et al., 2005; Otto et

551 al., 2006). Our previous work (Combe et al., 2018), showed that the SK current limited the spiking
552 frequency of CA1 pyramidal cells in response to trains of Schaffer collateral stimulation. Action
553 potentials failed on average for every other stimulus for > 50 Hz train in control, and blocking SK
554 with apamin allowed the cells to follow the stimulus train more faithfully. However, at the firing
555 frequencies (< 25 Hz) examined in this study, the SK K^+ current did not significantly contribute to
556 adaptation (Figure 3A). In addition, blocking the M-type K^+ current with XE-991, allowed the initial
557 spiking frequency to increase, but did not shift the spike ratio in our experiments (Figure 3B).
558 Similarly, linopirdine, a specific M-type channel blocker, changed the time course of spike
559 frequency adaptation in CA1 pyramidal cells, but not the degree of adaptation attained at steady
560 state (Fernandez and White, 2010). In either case, if only one current was blocked, it appeared
561 the other could compensate during the AHP, resulting in little effect on adaptation; on the other
562 hand, combined SK and M-type K^+ current block increased adaptation, as visible from the
563 increased spike ratio in the presence of apamin and XE-991 (Figure 3F). This counterintuitive
564 effect may be due to a shallower after-hyperpolarization that 1) led to a general increase in
565 excitability, allowing for a greater number of action potentials on the up-ramp and/or 2) removed
566 less Na_V inactivation, and therefore ultimately decreased the fast pool.

567 *Modulation*

568 We have shown that adaptation can be modulated by phosphorylation state (Figure 6).
569 Since phosphorylation states depend on the neuromodulatory milieu, adaptation may be plastic,
570 which is relevant to spatial navigation; increasing adaptation moves the center of mass of the
571 place field in a direction opposite the direction of motion, whereas decreasing adaptation moves
572 it in the direction of motion. As stated above, there are also implications for gain control of the
573 frequency-current relationship. Although we have modeled the transition rates between Markov
574 states as parameters, in the context of neuromodulation the transition rates can be considered
575 state variables whose values depend on the phosphorylation state of the channels.

576 *Generality of this mechanism of spike rate adaptation*

577 Adaptation due to long-term inactivation of Na_V channels has been observed in
578 serotonergic raphe neurons (Navarro et al., 2020). Long-term inactivation of Na_V channels has
579 also recently been demonstrated to control not only adaptation, but also entry into depolarization
580 block in midbrain dopamine neurons (Knowlton et al., 2021). We conclude that long-term
581 inactivation of Na_V channels may be quite generally utilized as a mechanism for spike frequency
582 adaptation in the central nervous system.

583

584 **References**

585 Aiken SP, Lampe BJ, Murphy PA, Brown BS (1995) Reduction of spike frequency adaptation and
586 blockade of M-current in rat CA1 pyramidal neurones by linopirdine (DuP 996), a neurotransmitter
587 release enhancer. Br J Pharmacol 115:1163–1168.

588 Ashhad S, Narayanan R (2013) Quantitative interactions between the A-type K+ current and
589 inositol trisphosphate receptors regulate intraneuronal Ca2+ waves and synaptic plasticity. J
590 Physiol 591:1645–1669.

591 Balbi P, Massobrio P, Hellgren Kotaleski J (2017) A single Markov-type kinetic model accounting
592 for the macroscopic currents of all human voltage-gated sodium channel isoforms. PLoS Comput
593 Biol 13:e1005737.

594 Baranauskas G, Martina M (2006) Sodium currents activate without a Hodgkin-and-Huxley-type
595 delay in central mammalian neurons. J Neurosci 26:671–684.

596 Bianchi D, Marasco A, Limongiello A, Marchetti C, Marie H, Tirozzi B, Migliore M (2012) On the
597 mechanisms underlying the depolarization block in the spiking dynamics of CA1 pyramidal
598 neurons. J Comput Neurosci 33:207–225.

599 Bittner KC, Grienberger C, Vaidya SP, Milstein AD, Macklin JJ, Suh J, Tonegawa S, Magee JC
600 (2015) Conjunctive input processing drives feature selectivity in hippocampal CA1 neurons. Nat
601 Neurosci 18:1133–1142.

602 Burgess N, Maguire EA, O'Keefe J (2002) The Human Hippocampus and Spatial and Episodic
603 Memory. Neuron 35:625–641.

604 Chance FS, Abbott LF, Reyes AD (2002) Gain modulation from background synaptic input.
605 Neuron 35:773–782.

606 Chen X, Johnston D (2005) Constitutively active G-protein-gated inwardly rectifying K+ channels
607 in dendrites of hippocampal CA1 pyramidal neurons. J Neurosci 25:3787–3792.

608 Cohen J (1977) CHAPTER 1 - The Concepts of Power Analysis. In: Statistical Power Analysis for
609 the Behavioral Sciences (Revised Edition), pp.1–17. Academic Press. Available at:
610 https://www.sciencedirect.com/science/article/pii/B9780121790608500062.

611 Colbert CM, Johnston D (1998) Protein kinase C activation decreases activity-dependent
612 attenuation of dendritic Na+ current in hippocampal CA1 pyramidal neurons. J Neurophysiol
613 79:491–495.

614 Colbert CM, Magee JC, Hoffman DA, Johnston D (1997) Slow recovery from inactivation of Na+
615 channels underlies the activity-dependent attenuation of dendritic action potentials in
616 hippocampal CA1 pyramidal neurons. The Journal of Neuroscience 17:6512–6521.

617 Colgin LL, Moser EI, Moser M-B (2008) Understanding memory through hippocampal remapping.
618 Trends Neurosci 31:469–477.

619 Combe CL, Canavier CC, Gasparini S (2018) Intrinsic Mechanisms of Frequency Selectivity in
620 the Proximal Dendrites of CA1 Pyramidal Neurons. J Neurosci 38:8110–8127.

621 Dover K, Solinas S, D'Angelo E, Goldfarb M (2010) Long-term inactivation particle for voltage-
622 gated sodium channels. The Journal of Physiology 588:3695–3711.

623 Epsztein J, Brecht M, Lee AK (2011) Intracellular determinants of hippocampal CA1 place and
624 silent cell activity in a novel environment. Neuron 70:109–120.

625 Fernandez FR, White JA (2010) Gain control in CA1 pyramidal cells using changes in somatic
626 conductance. The Journal of Neuroscience 30:230–241.

627 Fleidervish IA, Friedman A, Gutnick MJ (1996) Slow inactivation of Na+ current and slow
628 cumulative spike adaptation in mouse and guinea-pig neocortical neurones in slices. The Journal
629 of Physiology 493:83–97.

630 Fleidervish IA, Gutnick MJ (1996) Kinetics of slow inactivation of persistent sodium current in layer
631 V neurons of mouse neocortical slices. J Neurophysiol 76:2125–2130.

632 Fortin NJ, Agster KL, Eichenbaum HB (2002) Critical role of the hippocampus in memory for
633 sequences of events. Nature Neuroscience 5:458–462.

634 Gasparini S, Migliore M (2015) Action Potential Backpropagation. In: Encyclopedia of
635 Computational Neuroscience (Jaeger D, Jung R, eds), pp.133–137. New York, NY: Springer.
636 Available at: https://doi.org/10.1007/978-1-4614-6675-8_123.

637 Goldfarb M (2012) Voltage-gated sodium channel-associated proteins and alternative
638 mechanisms of inactivation and block. Cellular and molecular life sciences : CMLS 69 Available
639 at: https://pubmed.ncbi.nlm.nih.gov/21947499/.

640 Gu N, Hu H, Vervaeke K, Storm JF (2008) SK (KCa2) channels do not control somatic excitability
641 in CA1 pyramidal neurons but can be activated by dendritic excitatory synapses and regulate their
642 impact. J Neurophysiol 100:2589–2604.

Gu N, Vervaeke K, Hu H, Storm JF (2005) Kv7/KCNQ/M and HCN/h, but not KCa2/SK channels, contribute to the somatic medium after-hyperpolarization and excitability control in CA1 hippocampal pyramidal cells. The Journal of Physiology 566:689–715.

Hargreaves EL, Yoganarasimha D, Knierim JJ (2007) Cohesiveness of spatial and directional representations recorded from neural ensembles in the anterior thalamus, parasubiculum, medial entorhinal cortex, and hippocampus. Hippocampus 17:826–841.

Harris KD, Henze DA, Hirase H, Leinekugel X, Dragoi G, Czurkó A, Buzsáki G (2002) Spike train dynamics predicts theta-related phase precession in hippocampal pyramidal cells. Nature 417:738–741.

Harvey CD, Collman F, Dombeck DA, Tank DW (2009) Intracellular dynamics of hippocampal place cells during virtual navigation. Nature 461:941–946.

Hoang LT, Kesner RP (2008) Dorsal hippocampus, CA3, and CA1 lesions disrupt temporal sequence completion. Behavioral Neuroscience 122:9.

Hoffman DA, Johnston D (1998) Downregulation of Transient K+ Channels in Dendrites of Hippocampal CA1 Pyramidal Neurons by Activation of PKA and PKC. J Neurosci 18:3521–3528.

Hoffman DA, Magee JC, Colbert CM, Johnston D (1997) K+ channel regulation of signal propagation in dendrites of hippocampal pyramidal neurons. Nature 387:869–875.

Hunsaker MR, Thorup JA, Welch T, Kesner RP (2006) The role of CA3 and CA1 in the acquisition of an object-trace-place paired-associate task. Behavioral Neuroscience 120:1252.

Ishizuka N, Cowan WM, Amaral DG (1995) A quantitative analysis of the dendritic organization of pyramidal cells in the rat hippocampus. J Comp Neurol 362:17–45.

664 Jung H-Y, Mickus T, Spruston N (1997) Prolonged Sodium Channel Inactivation Contributes to
665 Dendritic Action Potential Attenuation in Hippocampal Pyramidal Neurons. J Neurosci 17:6639–
666 6646.

667 Kim J, Wei D-S, Hoffman DA (2005) Kv4 potassium channel subunits control action potential
668 repolarization and frequency-dependent broadening in rat hippocampal CA1 pyramidal neurones.
669 J Physiol 569:41–57.

670 Kirizs T, Kerti-Szigeti K, Lorincz A, Nusser Z (2014) Distinct axo-somato-dendritic distributions of
671 three potassium channels in CA1 hippocampal pyramidal cells. The European Journal of
672 Neuroscience 39:1771–1783.

673 Knowlton CJ, Ziouziou TI, Hammer N, Roeper J, Canavier CC (2021) Inactivation mode of sodium
674 channels defines the different maximal firing rates of conventional versus atypical midbrain
675 dopamine neurons. PLOS Computational Biology e1009371.

676 Liu PW, Bean BP (2014) Kv2 channel regulation of action potential repolarization and firing
677 patterns in superior cervical ganglion neurons and hippocampal CA1 pyramidal neurons. J
678 Neurosci 34:4991–5002.

679 Lorincz A, Nusser Z (2010) Molecular Identity of Dendritic Voltage-Gated Sodium Channels.
680 Science 328:906–909.

681 Madison DV, Nicoll RA (1984) Control of the repetitive discharge of rat CA 1 pyramidal neurones
682 in vitro. J Physiol 354:319–331.

683 Magee J, Hoffman D, Colbert C, Johnston D (1998) Electrical and calcium signaling in dendrites
684 of hippocampal pyramidal neurons. Annu Rev Physiol 60:327–346.

Magee JC (1998) Dendritic hyperpolarization-activated currents modify the integrative properties of hippocampal CA1 pyramidal neurons. J Neurosci 18:7613–7624.

Megías M, Emri Z, Freund TF, Gulyás AI (2001) Total number and distribution of inhibitory and excitatory synapses on hippocampal CA1 pyramidal cells. Neuroscience 102:527–540.

Mehta MR, Quirk MC, Wilson MA (2000) Experience-dependent asymmetric shape of hippocampal receptive fields. Neuron 25:707–715.

Mickus T, Jung H y, Spruston N (1999) Properties of slow, cumulative sodium channel inactivation in rat hippocampal CA1 pyramidal neurons. Biophys J 76:846–860.

Morgan PJ, Bourboulou R, Filippi C, Koenig-Gambini J, Epsztein J (2019) Kv1.1 contributes to a rapid homeostatic plasticity of intrinsic excitability in CA1 pyramidal neurons in vivo. Elife 8:e49915.

Navarro MA, Salari A, Lin JL, Cowan LM, Penington NJ, Milescu M, Milescu LS (2020) Sodium channels implement a molecular leaky integrator that detects action potentials and regulates neuronal firing. Elife 9.

O'Keefe J, Dostrovsky J (1971) The hippocampus as a spatial map. Preliminary evidence from unit activity in the freely-moving rat. Brain Res 34:171–175.

O'Keefe J, Nadel L (1978) The Hippocampus as a Cognitive Map. Oxford : New York: Oxford University Press.

Otto JF, Yang Y, Frankel WN, White HS, Wilcox KS (2006) A spontaneous mutation involving Kcnq2 (Kv7.2) reduces M-current density and spike frequency adaptation in mouse CA1 neurons. J Neurosci 26:2053–2059.

706 Pedarzani P, McCutcheon JE, Rogge G, Jensen BS, Christophersen P, Hougaard C, Strøbaek
707 D, Stocker M (2005) Specific enhancement of SK channel activity selectively potentiates the
708 afterhyperpolarizing current I(AHP) and modulates the firing properties of hippocampal pyramidal
709 neurons. J Biol Chem 280:41404–41411.

710 Peters HC, Hu H, Pongs O, Storm JF, Isbrandt D (2005) Conditional transgenic suppression of M
711 channels in mouse brain reveals functions in neuronal excitability, resonance and behavior. Nat
712 Neurosci 8:51–60.

713 Poirazi P, Brannon T, Mel BW (2003a) Arithmetic of subthreshold synaptic summation in a model
714 CA1 pyramidal cell. Neuron 37:977–987.

715 Poirazi P, Brannon T, Mel BW (2003b) Pyramidal Neuron as Two-Layer Neural Network. Neuron
716 37:989–999.

717 Resnik E, McFarland JM, Sprengel R, Sakmann B, Mehta MR (2012) The effects of GluA1
718 deletion on the hippocampal population code for position. J Neurosci 32:8952–8968.

719 Salinas E, Thier P (2000) Gain Modulation: A Major Computational Principle of the Central
720 Nervous System. Neuron 27:15–21.

721 Shah MM, Migliore M, Valencia I, Cooper EC, Brown DA (2008) Functional significance of axonal
722 Kv7 channels in hippocampal pyramidal neurons. Proc Natl Acad Sci U S A 105:7869–7874.

723 Shors TJ (2004) Memory traces of trace memories: neurogenesis, synaptogenesis and
724 awareness. Trends Neurosci 27:250–256.

725 Stocker M, Krause M, Pedarzani P (1999) An apamin-sensitive Ca2+-activated K+ current in
726 hippocampal pyramidal neurons. PNAS 96:4662–4667.

727 Ulbricht W (2005) Sodium Channel Inactivation: Molecular Determinants and Modulation.
728 Physiological Reviews 85:1271–1301.

729 Venugopal S, Hsiao C-F, Sonoda T, Wiedau-Pazos M, Chandler SH (2015) Homeostatic
730 dysregulation in membrane properties of masticatory motoneurons compared with oculomotor
731 neurons in a mouse model for amyotrophic lateral sclerosis. J Neurosci 35:707–720.

732 Wood ER, Dudchenko PA, Eichenbaum H (1999) The global record of memory in hippocampal
733 neuronal activity. Nature 397:613–616.

734 Zbili M, Debanne D (2020) Myelination Increases the Spatial Extent of Analog-Digital Modulation
735 of Synaptic Transmission: A Modeling Study. Front Cell Neurosci 14 Available at:
736 https://www.frontiersin.org/articles/10.3389/fncel.2020.00040/full#B34.

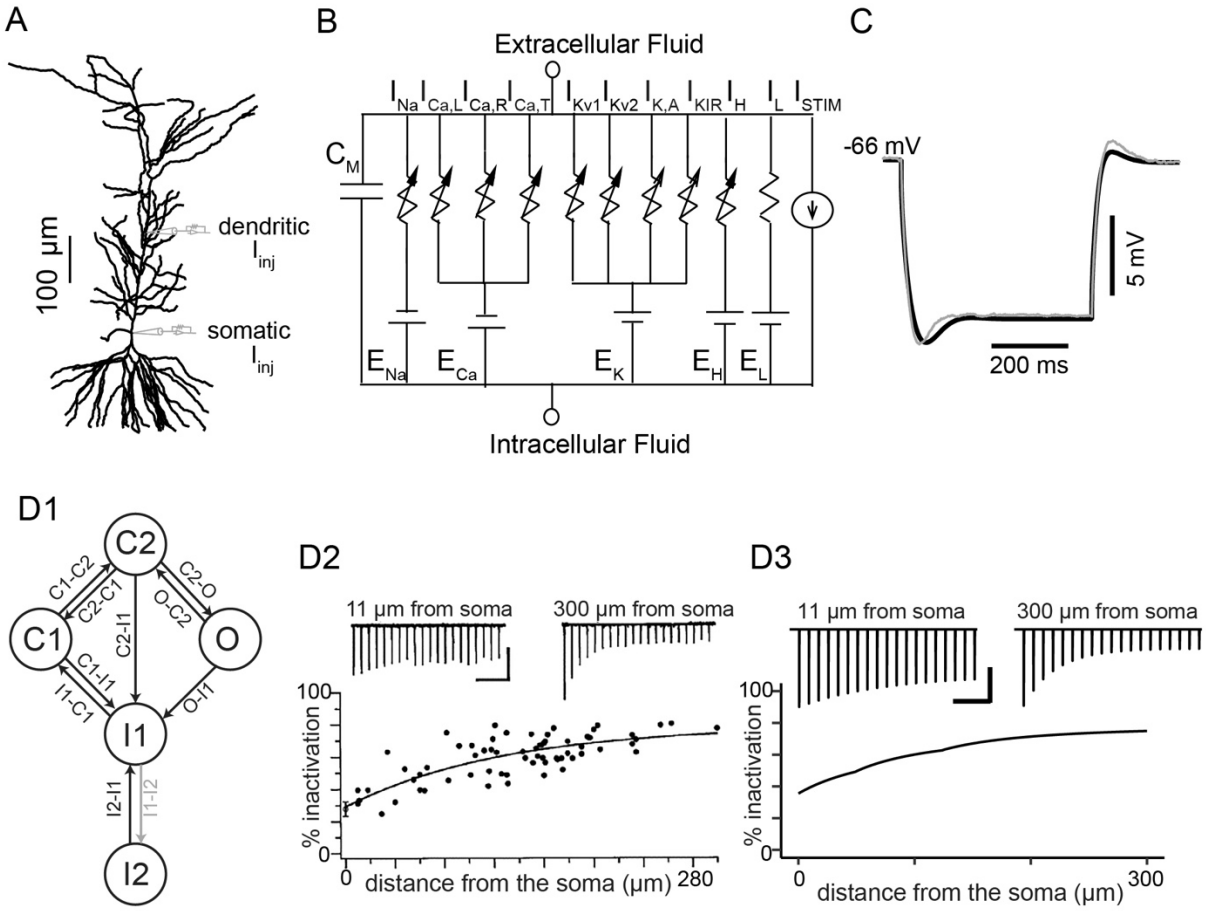

Figure 1. Model Schematic and Calibration. A. Morphology as implemented in the simulation package NEURON, showing the location of simulated current injection. Stimulus current was only injected either in the soma or apical trunk (219 µm from the soma). B. Circuit diagram for each compartment. C. Superimposed voltage traces resulting from a 500 ms, 200 pA hyperpolarizing step recorded experimentally (gray) or upon simulation (black) to determine the neuron input resistance. D. Sodium current model and calibration. D1. Five-state Markov model for NaV1.6; transition from the I1 to the I2 state is drawn in gray for emphasis. D2. Data on percent steady state sodium channel inactivation along the apical dendrite in CA1 pyramidal cells, slightly modified with permission from Figure 3B in the complete Elsevier source (Mickus et al., 1999). D3. Simulations were calibrated to fall within the envelope of the data in D2. Scale bars in D2 and D3 are 200 ms (horizontal) and 50 pA (vertical).

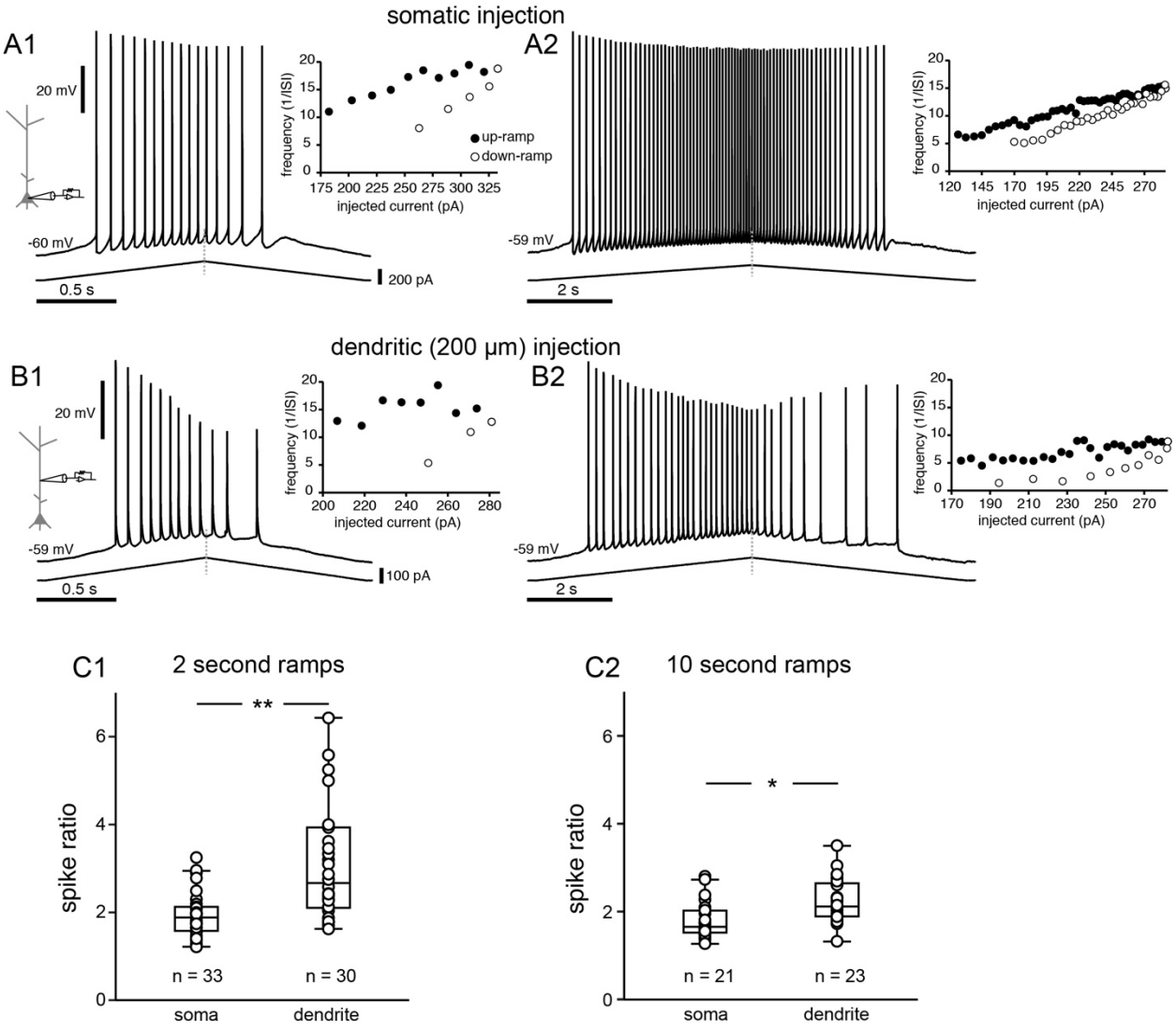

Figure 2. Asymmetric responses to symmetric triangular current ramps. A. Somatic injection. A1. Voltage trace recorded in the soma for a two second triangular current ramp injected in the soma. The inset shows the reciprocal of the interspike interval plotted versus the current injected at the midpoint of the interval; filled and open circles indicate interspike intervals on the up- and down-ramps, respectively. A2. Same as A1 but for a ten second ramp. B. Dendritic injection. B1. Voltage trace recorded for a two second triangular current ramp injected in the apical dendrite at about 200 µm from the soma. B2. Same as B1 but for a ten second ramp. C. Summary data of the ratio of spikes on the up-ramp to spikes on the down-ramp for two second (C1) and 10 second (C2) ramps are represented as box and whisker plots. The

759 number of recordings is indicated for each group; all ratios are greater than one, indicating more

760 action potentials on the up-ramp. * $p = 0.003$; ** $p < 0.001$

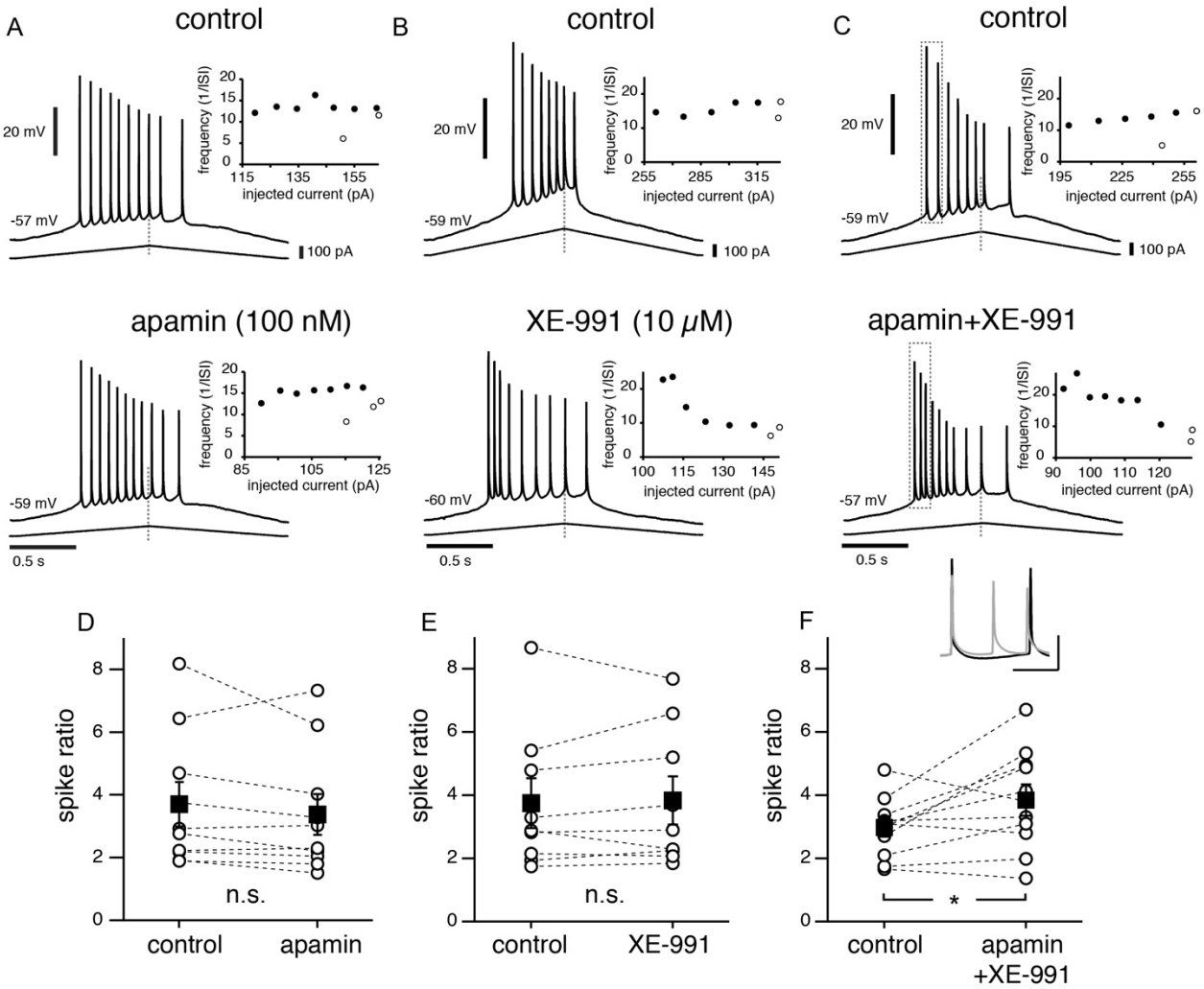

Figure 3. No clear effect of SK or M-type K^+ channel block on asymmetry of ramp responses in the dendrites. Recordings were obtained at approximately 200 μm from the soma along the apical dendrite. A. Voltage trace recorded in the apical dendrite for a two second triangular current ramp (shown beneath the voltage trace) injected in the apical dendrite in control (top) and in the presence of apamin (100 nM, bottom). Insets show the reciprocal of the interspike interval plotted versus the applied current at the midpoint of the interval as in Figure 2. B. Same as A for XE-991 10 μM. C. Same as A for the combined effects of apamin 100 nM and XE-991 10 μM. D-F. Spike ratio summary data for n = 10 neurons for apamin (D), n = 9 neurons for XE991 (E) and n = 11 for apamin + XE (F). The inset above F shows expanded traces, with first spikes aligned, from the areas indicated by the dotted boxes above (black control, gray in apamin+XE-991; scalebars

772 20 mV vertical and 50 ms horizontal). Dotted lines connect individual cells before and after
773 addition of drug. Black squares with error bars represent group averages ± SEM. n.s. not
774 significant; * denotes $p < 0.05$.

775

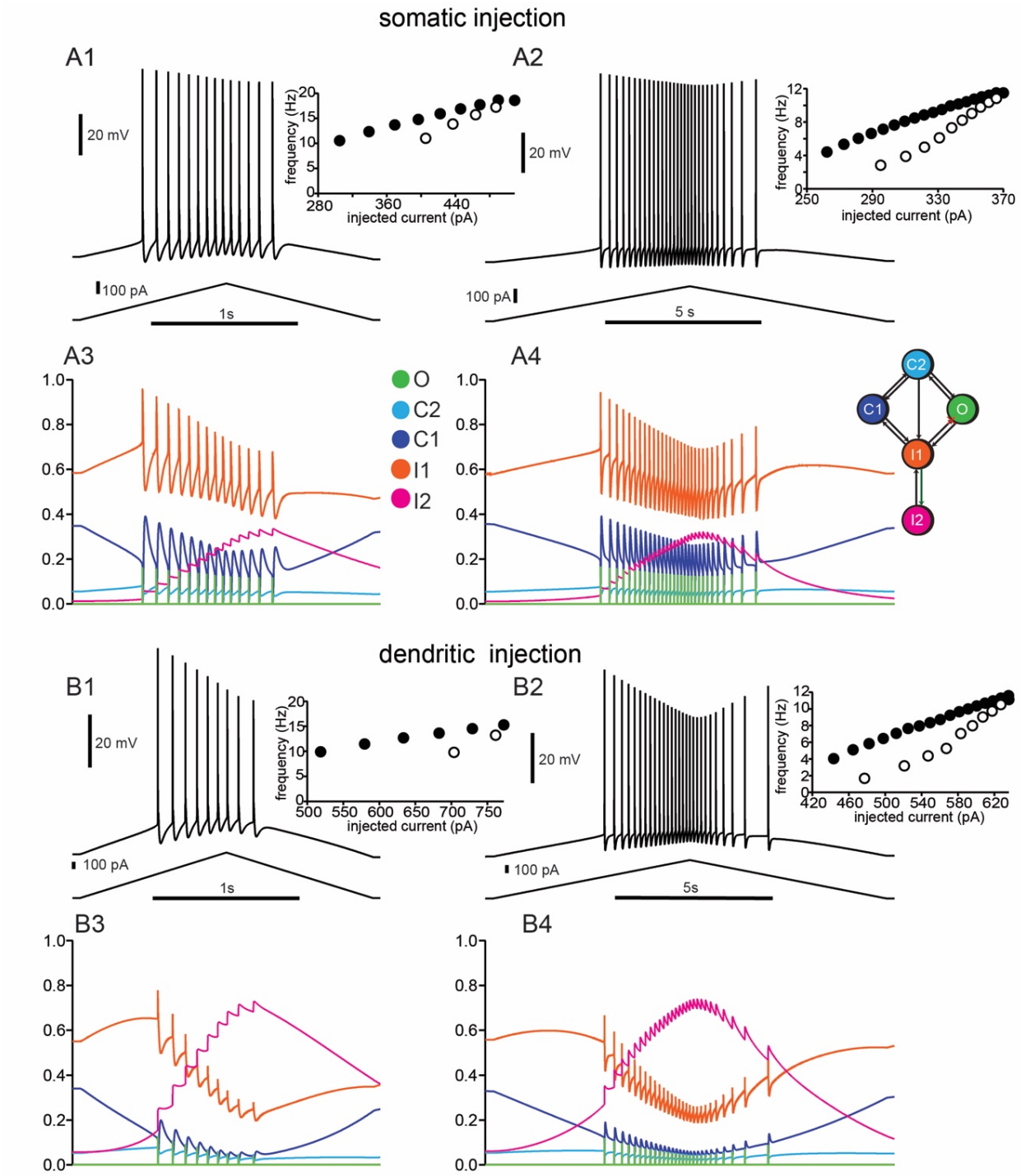

Figure 4. Model captures differences in somatic and dendritic responses in terms of Na_V availability. A. Simulated voltage traces and the resulting occupancy in each state of the Na_V Markov model for current ramps injected at the soma. A1. Somatic voltage response to a two

second current ramp (shown beneath the voltage trace). A2. Somatic voltage response to a ten second current ramp (shown beneath the voltage trace). Insets are as in previous figures. Color plots depict the state occupancy for the corresponding two second ramp (A3) and ten second ramp (A4) and are color coded to match the Markov model schematic at right. B. Simulated voltage traces and resulting state occupancy for current ramps injected in the apical trunk at 219 microns from the soma. B1. Dendritic voltage response to a two second current ramp. B2. Dendritic voltage response to a ten second current ramp. Color plots of state occupancy (B3 and B4) correspond to the two second dendritic injection and ten second dendritic injection, respectively.

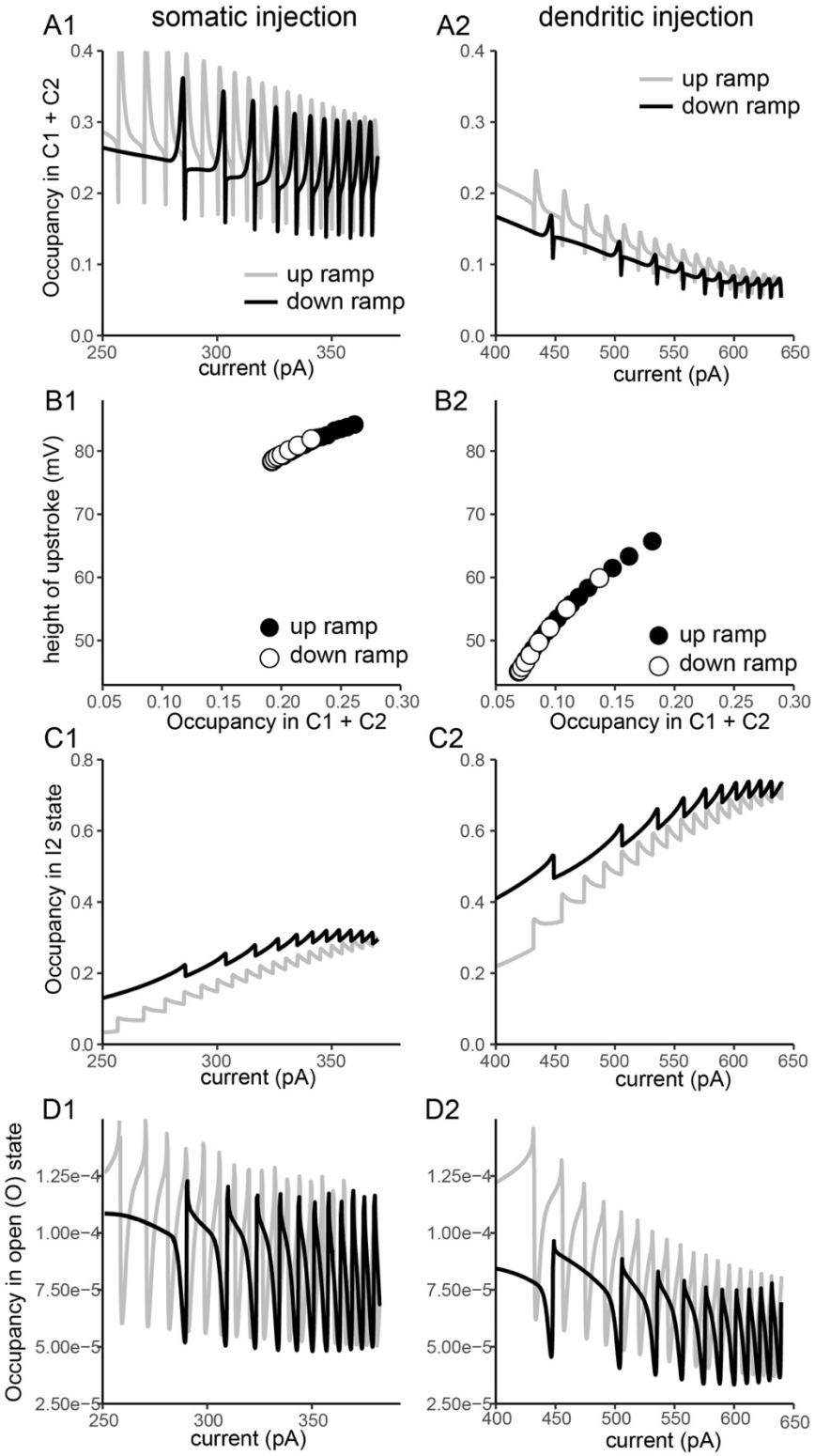

789

790 **Figure 5. Differential regulation of spike amplitude and frequency arises from differences**

791 **in Na_V availability during ten second current ramp.** Different parameters measured during

792 somatic injection are shown on the left and dendritic injection on the right. A. Hysteresis in
793 occupancy in the available pool of C1+C2 is visible during the ten second ramp, with availability
794 generally lower on the down-ramp (black) than on the up-ramp (gray). B. Occupancy in the
795 available pool (C1+C2) at spike threshold is strongly predictive of spike height, measured from
796 threshold to peak, irrespective of ramp direction (up, filled circles; down, open circles). C.
797 Hysteresis in occupancy in the slow, unavailable pool (I2) shows that inactivation is generally
798 higher on the down-ramp (black) than on the up-ramp (gray). D. Hysteresis in occupancy in the
799 open state, with higher occupancy on the up-ramp than the down-ramp, explains the lower
800 frequencies on the down-ramp. Values of occupancy during the spike were truncated for clarity
801 to better show the very small open fraction during the interspike intervals.

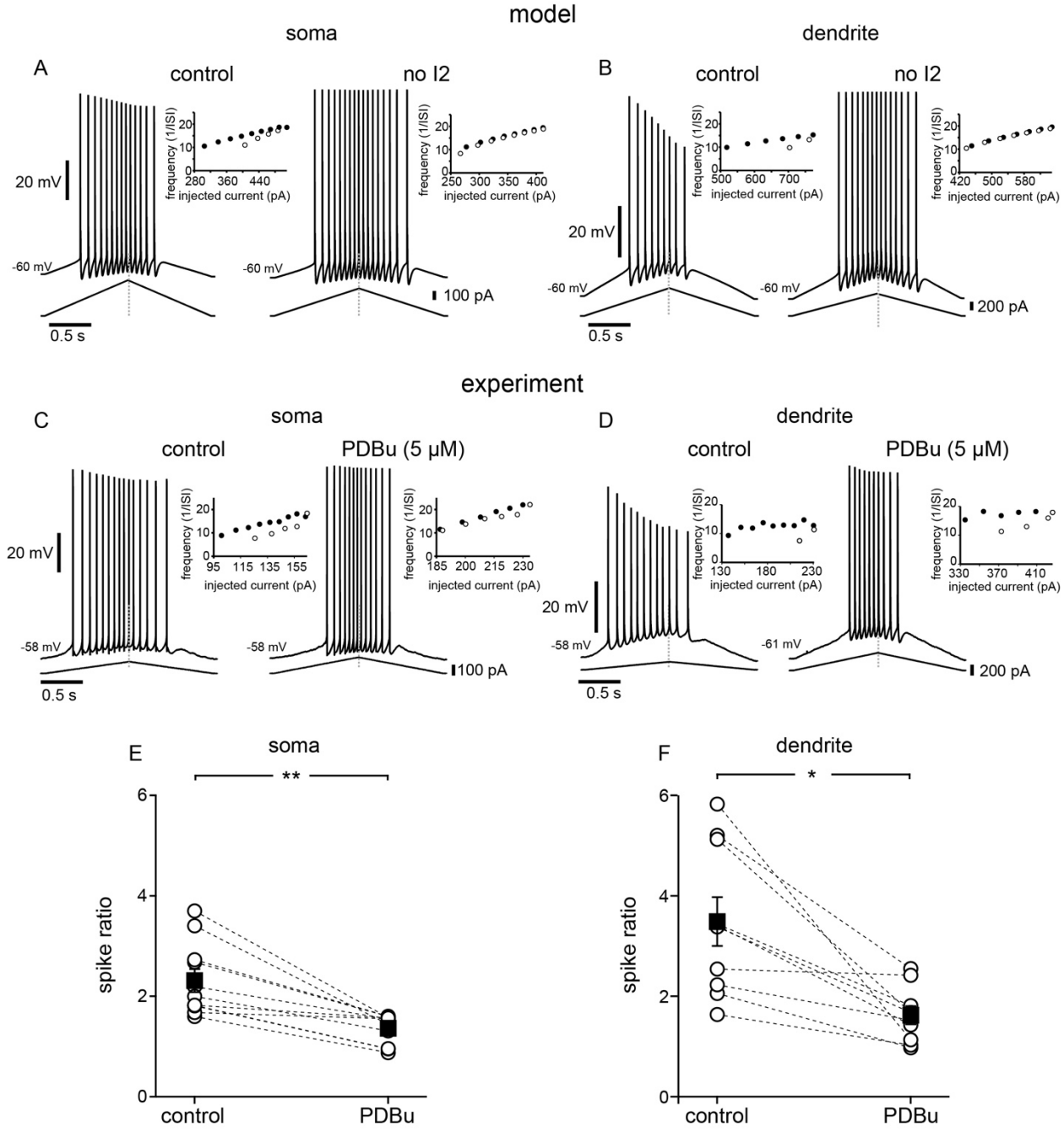

Figure 6. The model predicts and experiments confirm that reducing long-term inactivation reduces adaptation and asymmetry. A. Simulations of somatic current injection in control and with the I1 to I2 transition rate set to zero, meaning there is no occupancy in the long-term inactivated state. The insets show that adaptation and asymmetry are essentially eliminated by this manipulation, producing a linear f/I curve. B. Simulations of dendritic current injection in

808 control and with the I1 to I2 transition rate set to zero. Controls in A and B are repeated from
809 Figure 4; stimulus current was injected either in the soma or apical trunk (219 μm from the soma).
810 C. Example experimental traces showing the voltage response to somatic current ramp injection
811 in control and with 5 μM PDBu. D. Example experimental traces for dendritic current injection
812 before and after addition of 5 μM PDBu. E. Summary spike ratio data for soma (n = 11). F.
813 Summary spike ratio data for dendritic ramps (n = 10). Dotted lines connect individual cell
814 averages before and after addition of drug. Black squares with error bars represent group
815 averages ± SEM. ** $p < 0.001$; * $p = 0.002$.

816

817 Figure 6-1. Extended data for Figure 6 with an alternate morphology. A. Simulations of somatic
818 current injection in control (A1) and with the I1 to I2 transition rate set to zero (A2). The insets
819 show that adaptation and asymmetry are essentially eliminated by this manipulation, producing a
820 linear f/I curve. B. Simulations of dendritic current injection (at 192 μm from the soma) in control
821 (B1) and with the I1 to I2 transition rate set to zero (B2). C) Morphology
822 (http://neuromorpho.org/neuron_info.jsp?neuron_name=c80761 from (Ishizuka et al., 1995) as
823 implemented in the simulation package NEURON, showing the location of simulated current
824 injection. The point where the apical dendrite branches into the tuft is at 388 μm from the soma
825 in this case. Stimulus current was injected either in the soma or apical trunk.

826

827 Figure 6-2. Extended data for Figure 6 with a second alternate morphology. A. Simulations of
828 somatic current injection in control (A1) and with the I1 to I2 transition rate set to zero (A2). The
829 insets show that adaptation and asymmetry are essentially eliminated by this manipulation,
830 producing a linear f/I curve. B. Simulations of dendritic current injection (at 208 μm from the soma)
831 in control (B1) and with the I1 to I2 transition rate set to zero (B2). C) Morphology

(http://neuromorpho.org/neuron_info.jsp?neuron_name=pc1a from Megías et al., 2001) as implemented in the simulation package NEURON, showing the location of simulated current injection. The point where the apical dendrite branches into the tuft is at 343 μm from the soma in this case. Stimulus current was injected either in the soma or apical trunk. In this case, the percent of inactivation in the model (see Figure 1D3) was uniformly decreased by 5% to increase firing with dendritic injection; the resulting plot was still in the envelope of the experimental data (see Figure 1D2).

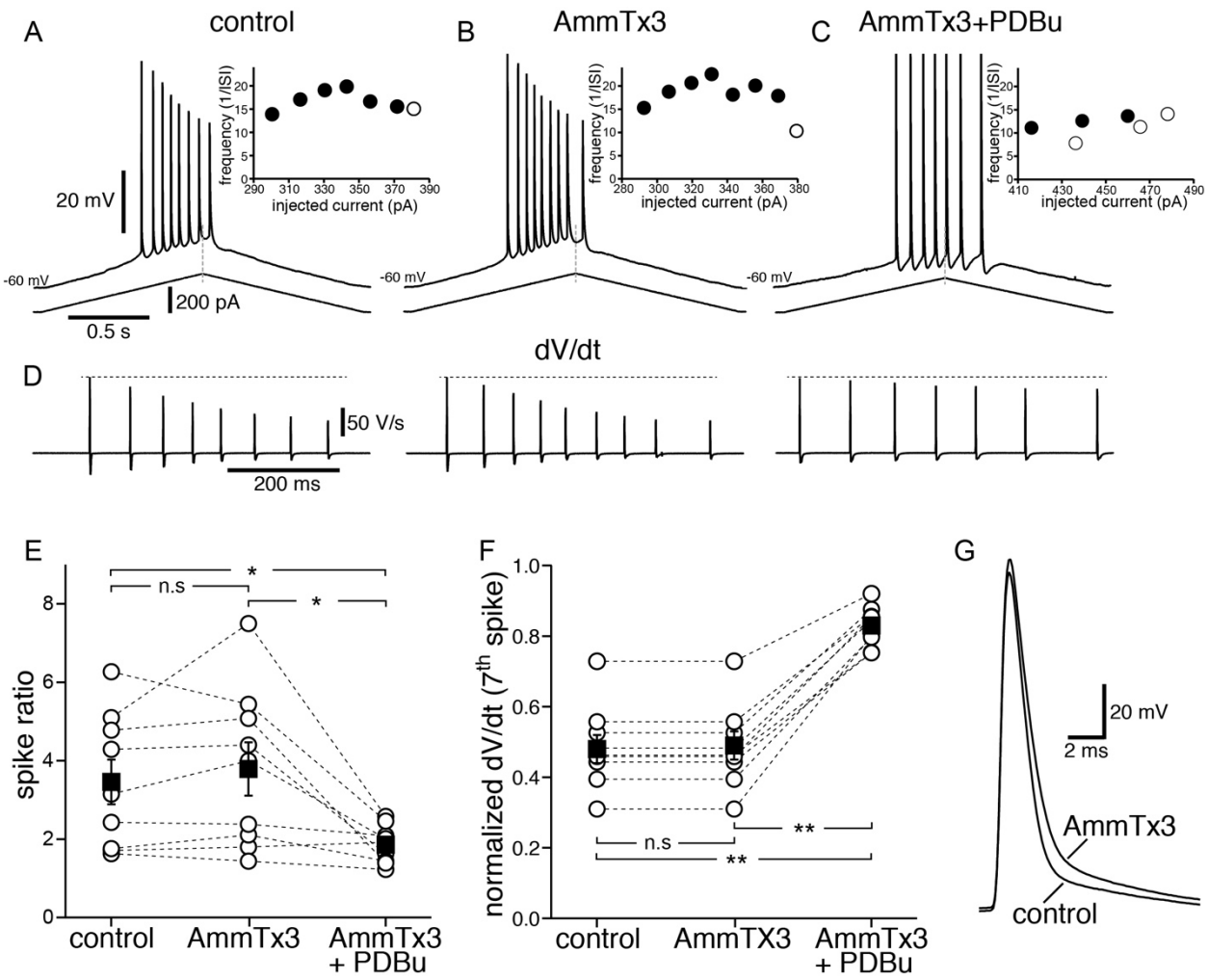

Figure 7 PKC phosphorylation of Kv4 channels does not mediate the reduction in adaptation and asymmetry due to phorbol ester. Top. Two second dendritic ramps. Voltage traces, current ramps and f/I curve are as in Figures 2-4. A Control. B. AmmTx3 (300 nM) added to the bath. C. PDBu (5μM) in addition to AmmTx3. D. Traces at the bottom show the first temporal derivative of the voltage trace. E. Summary data for spike ratios. ** $p < 0.001$; * $p < 0.05$; n.s. not significant. F. Normalized peak first temporal derivative for seventh spike. G. AmmTx3 broadens the AP by slowing repolarization.

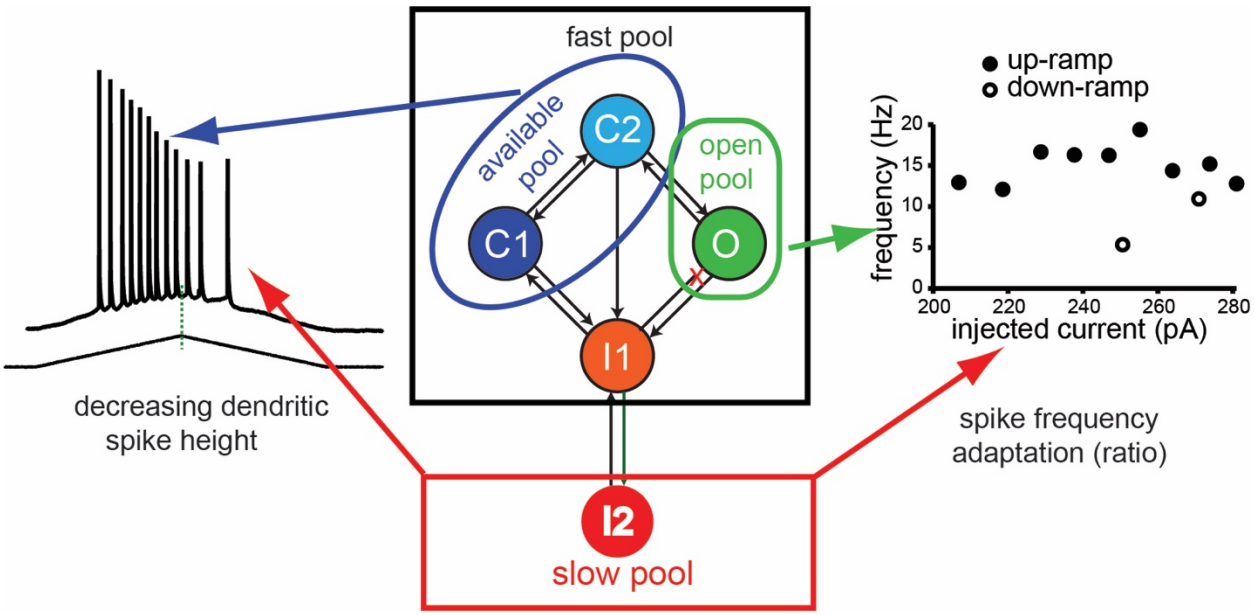

847

848 **Figure 8. Summary diagram of the contributions of the various occupancy states to spike**

849 **height (left) and adaptation/asymmetry.** Details are in the discussion.

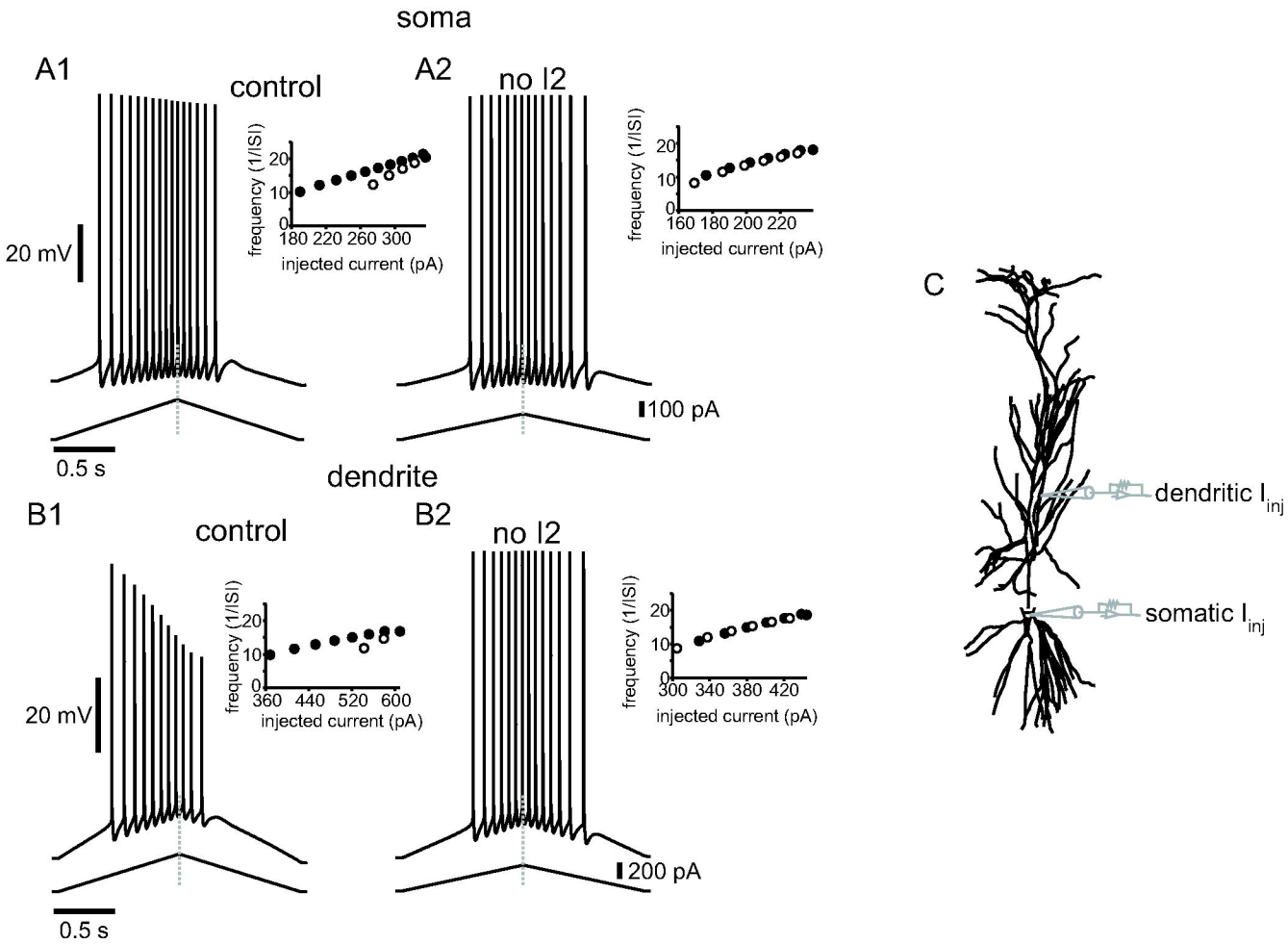
soma
A1
control
A2
no I2
20 mV
0.5 s
100 pA
frequency (1/ISI)
injected current (pA)
dendrite
B1
control
B2
no I2
20 mV
0.5 s
200 pA
C
dendritic I inj
somatic I inj

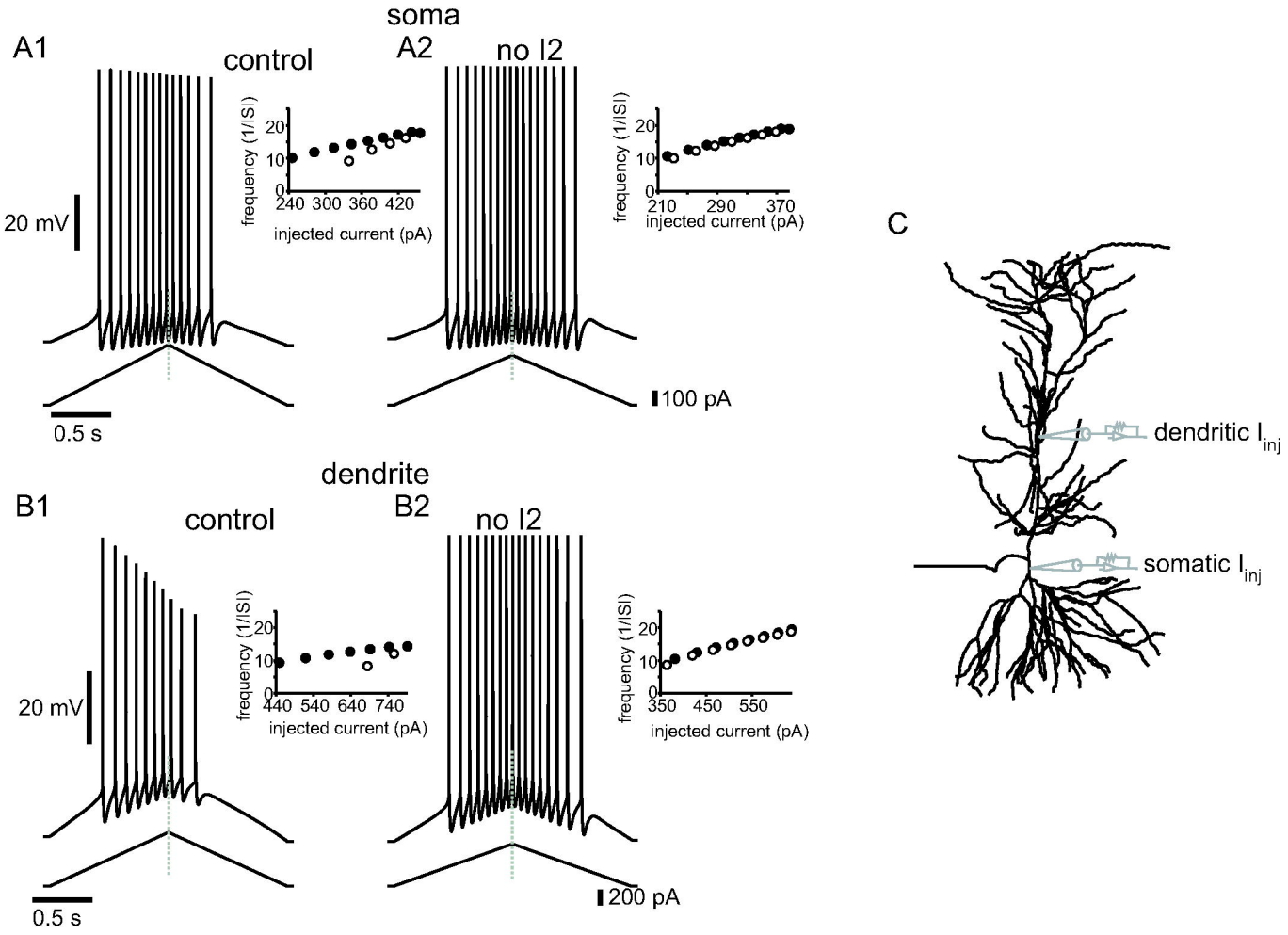
soma
A1
control
A2
no I2
20 mV
0.5 s
100 pA
frequency (1/ISI)
injected current (pA)
dendrite
B1
control
B2
no I2
20 mV
0.5 s
200 pA
C
dendritic I_{inj}
somatic I_{inj}